NASA TECHNICAL MEMORANDUM

NASA TM X-3368

NASA TM X-3368

SPACE SHUTTLE POGO ACTIVE CONTROLLER DESIGN USING FREQUENCY DOMAIN OPTIMIZATION

Robert C. Seidel, Carl F. Lorenzo, and Bruce Lehtinen

Lewis Research Center
Cleveland, Ohio 44135

NATIONAL AERONAUTICS AND SPACE ADMINISTRATION • WASHINGTON, D. C. • APRIL 1976

1. Report No.	2. Government Accession No.	3. Recipient's Catalog No.
NASA TM X-3368		

4. Title and Subtitle	5. Report Date
SPACE SHUTTLE POGO ACTIVE CONTROLLER DESIGN USING FREQUENCY DOMAIN OPTIMIZATION	April 1976
	6. Performing Organization Code
7. Author(s)	8. Performing Organization Report No.
Robert C. Seidel, Carl F. Lorenzo, and Bruce Lehtinen	E-8529
	10. Work Unit No.
9. Performing Organization Name and Address	505-05
Lewis Research Center	11. Contract or Grant No.
National Aeronautics and Space Administration	
Cleveland, Ohio 44135	13. Type of Report and Period Covered
12. Sponsoring Agency Name and Address	Technical Memorandum
National Aeronautics and Space Administration	14. Sponsoring Agency Code
Washington, D.C. 20546	

15. Supplementary Notes

16. Abstract

A frequency domain parameter optimization technique was used to design active pogo suppression controls for the space shuttle. The technique uses a conjugate gradient search procedure and is well suited for designing low-order controllers for higher order systems. The shuttle model was a two-pump and six-structural-mode linear model representing a worst-case condition. A promising feedback controller structure was found to be a lead-lag design.

17. Key Words (Suggested by Author(s))	18. Distribution Statement
Space shuttle; Pogo suppression; Controller design; Optimal control; Feedback control; Optimization	Unclassified - unlimited STAR Category 63 (rev.)

19. Security Classif. (of this report)	20. Security Classif. (of this page)	21. No. of Pages	22. Price*
Unclassified	Unclassified	39	$3.75

* For sale by the National Technical Information Service, Springfield, Virginia 22161

SPACE SHUTTLE POGO ACTIVE CONTROLLER DESIGN USING FREQUENCY DOMAIN OPTIMIZATION

by Robert C. Seidel, Carl F. Lorenzo, and Bruce Lehtinen

Lewis Research Center

SUMMARY

A frequency domain parameter optimization technique was used in a preliminary design study of active pogo suppression controls for the space shuttle. The technique uses a conjugate gradient search procedure to optimize a cost function of controller performance and is well suited for designing low-order controllers for higher order systems. The shuttle model was a two-pump and six-structural-mode linear model of order 41, representing a worst-case condition. The suction pressure of the high-pressure oxidizer pump was the controlled variable. The parameter optimization was performed for four different low-order controllers. The resulting closed-loop system performances were evaluated by several means including controller performance averaged square values, frequency responses, system damping ratios, and sensitivities to structural model changes. A promising feedback controller structure was found to be a lead-lag design.

INTRODUCTION

Liquid-propellant rocket vehicles can experience oscillations of thrust commonly known as pogo. The pogo problem results from interactions between the vehicle structural modes of vibration and the propulsion system modes. Two concepts applicable to the space shuttle suppress pogo by suppressing feedline flow changes. They are a passive accumulator and an active suppressor. The active suppressor consists of a piston type of device which injects and removes flow from the propulsion system based on a sensed signal (ref. 1). A critical element in an active suppressor is the feedback controller design which is the subject of this report.

The controller design uses a frequency-domain parameter optimization technique that is well suited for designing low-order controllers for higher order systems (ref. 2). The pogo model of the space shuttle is basically the Aerospace Corporation linear model

of references 3 and 4. At Lewis the model was cast into a matrix state variable model with multiple structural modes and lumped feedline description. Plant transfer functions were obtained from the matrix model using the computer programs of reference 5.

This report describes the control problem and discusses the design results. The control problem description includes a discussion of the shuttle model, the controller, and the parameter optimization technique. The results present controller performances (averaged square values) for four controller structures. Analysis of selected designs includes system frequency responses, eigenvalue damping ratios, and sensitivities to changes in structural mode natural frequencies.

SYMBOLS

b	controller parameter vector
b_1	b vector element proportional gain, dimensionless
b_2	b vector element derivative gain, dimensionless
b_3	b vector element lead-lag gain, dimensionless
b_4	b vector element lead-lag zero, rad/sec
b_5	b vector element second-order lead-lag gain, dimensionless
b_6	b vector element second-order lead-lag damping ratio, dimensionless
b_7	b vector element second-order lead-lag natural frequency, rad/sec
C	cost function, $(N/cm^2)^2$
D	power spectral density of d, $[cm^3/(sec \cdot rad)]^2$
d	disturbance in feedline, cm^3/sec
F	cost function value, $(N/cm^2)^2/(rad/sec)$
G	system open-loop transfer function, $(N/cm^2)/(cm^3/sec)$
G_a	actuator, cm^3/sec
G_{cl}	system closed-loop transfer function, $(N/cm^2)/(cm^3/sec)$
H	controller, $(cm^3/sec)/(N/cm^2)$
h	controller filter
$j\omega$	Fourier variable, 1/sec
K	pressure transducer gain, cm^2/N

K_a actuator gain, cm^3/sec

P_7 HPOP suction pressure variation, N/cm^2

Q_a suppressor flow, cm^3/sec

r weighting factor $[(N/cm^2)/(cm^3/sec)]^2$

s Laplace variable, 1/sec

t time, sec

V power spectral density of v, $[N/(cm^2 \cdot rad)]^2$

v measurement noise, N/cm^2

y variable

τ random noise averaging time, sec

ω angular frequency, rad/sec

ω_a suppressor actuator pole, rad/sec

Subscripts:

d excitation by d

$( )_N$ normalized value

v excitation by v

Superscripts:

$\bar{}$ frequency average

$\bar{=}$ time average

CONTROL PROBLEM DESCRIPTION

Description of Shuttle Model

A drawing of the space shuttle carrying the orbiter vehicle is shown in figure 1(a). The liquid-oxygen feed system dynamics can interact with the vehical structural dynamics to produce pogo. In figure 1(b) a schematic diagram is shown of the liquid oxygen part of the shuttle propulsion system that includes the liquid oxygen tank, feedline, low-pressure oxidizer pump (LPOP), the suppressor (under consideration herein), high-pressure oxidizer pump (HPOP), and the rocket chamber.

To obtain the (state variable matrix) model used in this report, two changes were made to the reference 3 model. The first change was to approximate the distributed parameter feedline equations with a number of lumped parameter approximations. The

feedline segment between stations 1 and 2 was divided into nine parts, and the segment between stations 2 and 3 was divided into three parts. The second change was to include six structural modes in the model simultaneously instead of only one mode, as was done in reference 3. This insured that a controller designed to stabilize one mode had no serious destabilizing effects on the remaining modes. A detailed discussion of the modified model is presented in the appendix.

The model of reference 3 has variable model parameters that change for different flight conditions. A nominally worst-case model was assumed for this control study to avoid studying all possible configurations in flight. The worst-case model is basically the reference 3 model at the end-burn conditions except for the following: the end-burn structural mode at 2.81 hertz was replaced by a less stable configuration which was the 2.3-hertz mode from the after-separation condition. The nominal 26-hertz structural mode was shifted to 24 hertz to make the system open-loop unstable. Also, the low- and high-pressure oxidizer pump gains $m_1 + 1$ and $m_2 + 1$ were set to the maximum expected value (over the flight time) of 2.20 and 1.54, respectively. The pump inlet bubble compliances were set to the minimum (end burn) values of $C_{b1} = 5.944$ centimeter^5 per newton (0.25 in.^{5}/lbf) and $C_{b2} = 2.376$ cm^5/N (0.10 in.^{5}/lbf).

Description of Control System

The control system structure assumed as a framework for the controller design problem is shown in figure 2. The plant is block G(s) (where s is the Laplace variable) and the plant output is P_7, a pressure perturbation from the nominal steady-state operating point of the HPOP suction pressure. This pressure variation is sensed and used as the system feedback signal. The suppressor considered in this study was located at the HPOP inlet. The proximity of the pressure measurement to the suppressor reduces plant phase lag and will generally result in better closed-loop control. The plant disturbance d is assumed to be a flow disturbance that enters the plant in parallel with the system suppressor flow Q_a (fig. 2) at station 7. This is compatible with the optimization program constraints. There is also a measurement noise signal v. The d and v signals are assumed to be independent Gaussian white noises with power spectral densities D and V, respectively.

The controller H(s, b) representation consists of three factors: a transducer gain K, a suppressor actuator transfer function $G_a(s)$, and a controller filter transfer function h(s, b). The filter includes a vector of variable parameters b to be determined as described in the section Parameter Optimization.

$$H(s,b) = Kh(s,b)G_a(s) \tag{1}$$

The suppressor actuator transfer function $G_a(s)$ was assumed to be a first-order lag with a pole ω_a and a steady-state gain K_a.

$$G_a(s) = \frac{K_a}{\frac{s}{\omega_a} + 1} \tag{2}$$

For the purposes of this study the following values were chosen for the controller constants:

$K = 1.450\ cm^2/N\ (1.000\ in.^2/lbf)$

$K_a = 16.39\ cm^3/sec\ (1.000\ in.^3/sec)$

$\omega_a = (2\pi)50\ rad/sec$

A more detailed design study should consider an actuator representation including higher order servovalve characteristics and saturation limits.

The purpose of the controller is to minimize the variation in the system pressures and flows due to the disturbance d. At the same time it is desirable to minimize the control effort to accomplish this Q_a. The pressure variation P_7 has been used in this study as an indicator of the system response.

The plant-transfer-function $G(s) = P_7(s)/d$ (of fig. 2) frequency-response magnitude and phase is plotted in figure 3. The response is for the multistructural-mode, worst-case model previously described. There are a number of resonances indicated by the magnitude and phase data. These include a very lightly damped mode at about 2.3 hertz and an unstable mode at about 24 hertz. The instability is not apparent from the separate frequency response plots, but the system can be seen to be unstable from an eigenvalue analysis.

The complex roots of the denominator of the plant transfer function set the plant resonances. The damping ratios and natural frequencies associated with the complex roots (the eigenvalues of the system matrix) are tabulated in table I. The natural frequencies associated with the uncoupled structural mode natural frequencies are footnoted. The uncoupled structural modes are assumed to have a damping ratio of 0.01 in the model. The coupling of the structural and propulsion system modes has reduced some system eigenvalue damping ratios. The mode at about 2.3 hertz has a damping ratio of only 0.0008. The unstable mode at about 24 hertz has a damping ratio of -0.0015.

The frequency range of major interest for the study is below 30 hertz as set by the highest structural mode at 26.8 hertz. There are low damping ratios for the frequencies above about 40 hertz. But these higher frequency modes are associated with the feedline and do not involve a pogo problem with the structural modes. The approximations made

to form a lumped parameter model of the feedline dynamics lose accuracy as frequency is increased.

Parameter Optimization

A cost function, defined here, reflects the average variations in P_7 and Q_a caused by the random disturbance and measurement noises d and v (fig. 2). The cost function C formulated was the mean square value of the pressure variation of P_7 plus the mean square value of the control effort Q_a weighted by scalar r.

$$C(b) = \lim_{\tau \to \infty} \frac{1}{2\tau} \int_{-\tau}^{\tau} \left[P_7(t,b)^2 + rQ_a(t,b)^2 \right] dt = \overline{\overline{P_7(b)^2}} + r\overline{\overline{Q_a(b)^2}} \tag{3}$$

where the double bar notation denotes a time average. By Parseval's theorem this cost function can be transferred out of the time domain and into the frequency domain where the parameter optimization calculations are made:

$$C(b) = \frac{1}{\pi} \int_0^{\infty} \left[\left| P_7(j\omega,b) \right|^2 + r \left| Q_a(j\omega,b) \right|^2 \right] d\omega = \frac{1}{\pi} \left[\overline{\left| P_7(b) \right|^2} + r \overline{\left| Q_a(b) \right|^2} \right] \tag{4}$$

where $j\omega$ is the Fourier variable, ω is angular frequency, and the bar notation denotes integration with respect to frequency. Because the inputs are independent and the system is linear, equation (4) can be expanded to express the individual effects of disturbance d and measurement noise v as,

$$C(b) = \frac{1}{\pi} \left[\overline{\left| P_7(b) \right|_d^2} + \overline{\left| P_7(b) \right|_v^2} + r \overline{\left| Q_a(b) \right|_d^2} + r \overline{\left| Q_a(b) \right|_v^2} \right] \tag{5}$$

where the subscripts d and v indicate the origin of the excitation.

As was done in reference 2, C is expressed in terms of transfer function relationships. The expression for C is obtained in terms of the following known quantities: the power spectral density D of the disturbance d, the power spectral density V of the measurement noise v, the plant transfer function G, and the controller transfer function H. To start, the system closed-loop transfer function G_{cl} between P_7 and d is the usual closed-loop feedback relationship:

$$G_{cl}(j\omega, b) = \frac{G(j\omega)}{1 + G(j\omega)H(j\omega, b)} \tag{6}$$

From block diagram algebra, we obtain

$$\left.\begin{aligned} |P_7(j\omega,b)|_d^2 &= D|G_{cl}(j\omega,b)|^2 \\ |P_7(j\omega,b)|_v^2 &= V|G_{cl}(j\omega,b)\cdot H(j\omega,b)|^2 \\ |Q_a(j\omega,b)|_d^2 &= D|G_{cl}(j\omega,b)\cdot H(j\omega,b)|^2 \\ |Q_a(j\omega,b)|_v^2 &= V|G_{cl}(j\omega,b)\cdot H(j\omega,b)/G(j\omega)|^2 \end{aligned}\right\} \tag{7}$$

and $C(b)$ may now be expressed as

$$C(b) = \frac{1}{\pi}\int_0^\infty F(\omega,b)d\omega \tag{8}$$

where, after substituting and combining terms, F is

$$F(\omega,b) = |G_{cl}(j\omega,b)|^2\left\{|H(j\omega,b)|^2\left[rD + V + \frac{rV}{|G(j\omega)|^2}\right] + D\right\} \tag{9}$$

With an equation from which to evaluate C as a function of known system relationships and variable controller parameter initial estimates b, the parameter optimization problem is to minimize $C(b)$ by the proper selection of parameter vector b. Most parameter optimization methods, including the conjugate gradient method (which is used here) require also that the gradient of $C(b)$ with respect to the parameter vector b be calculated. The gradient of $C(b)$ is obtained by taking the gradient of both sides of equation (8).

$$\nabla C(b) = \frac{1}{\pi}\int_0^\infty \nabla F(\omega,b)d\omega \tag{10}$$

Use is made of the identity

$$\nabla\left|y(j\omega)\right|^2 = 2\,Re\left[y(-j\omega)\nabla y(j\omega)\right]$$

and equation (9) to express $\nabla F(\omega, b)$ as

$$\nabla F(\omega,b) = 2\left|G_{cl}(j\omega,b)\right|^2 Re\left(\left\{H(-j\omega,b)\left[rD + V + \frac{rV}{\left|G(j\omega)\right|^2}\right] - DG(j\omega)\right\}\frac{G_{cl}(j\omega,b)}{G(j\omega)}\nabla H(j\omega,b)\right) \tag{11}$$

Once the structure for $H(j\omega,b)$ has been chosen and the values of b selected, the cost function and its gradient can be calculated.

The computer program which computes the cost function and the cost function gradient and which conducts the gradient search is basically the program from reference 2. The trapezoidal integration rule is used to evaluate the cost function and gradient integrals (eqs. (8) and (10)). The integration requires a (single) previous evaluation of the plant transfer function $G(j\omega)$ at discrete frequency points. For the pogo problem 219 points were selected over a frequency range of 0.5 to 114 hertz. The spacing of the frequency points is determined by the change in the open-loop plant, so that integration errors are minimal. In addition, a variable step size, incorporated in the reference 2 program, further reduces errors caused by a fixed step size when the closed-loop transfer function magnitude $\left|G_{cl}(j,b)\right|$ exceeds the open-loop transfer function magnitude $\left|G(j\omega)\right|$. The additional closed-loop points calculations are based on the interpolation of the neighboring open-loop data points. The controller parameters b in $h(s,b)$ are handled in factored form. A scaling of each parameter by its own magnitude leads to rapidly converging searches. The value of the cost function does not necessarily indicate whether the system is stable for the controller found by the search. System stability is determined by a Routh-Horwitz stability test on the system characteristic polynomial $1 + G(s)H(s,b)$ (using a subroutine obtained from ref. 6).

The computation time for a single evaluation of the cost function and gradient for a two-parameter controller was about 0.36 second for the computer used (IBM 360-67 TSS). A typical two-parameter search would usually converge in less than 10 iterations; thus, a parameter optimization could usually be performed in several seconds.

RESULTS

Controller Filter Structures

The best structure for the controller transfer function $h(s,b)$ is not known on starting a controller design. The best structure may be a compromise between low order for reasons of practical implementation and high order for improvement in control. The

controller structures reported here start at order zero and increase in complexity to order two. Four controller structures are considered:

(1) A proportional gain controller for which $h(s,b) = b_1$

(2) An approximate derivative controller for which

$$h(s,b) = \frac{b_2 s}{\left(\frac{s}{1000} + 1\right)}$$

(3) A lead-lag controller for which

$$h(s,b) = \frac{b_3\left(\frac{s}{b_4} + 1\right)}{\left(\frac{s}{1000} + 1\right)}$$

(4) A second-order lead-lag controller for which

$$h(s,b) = \frac{b_5\left(\frac{s^2}{b_7^2} + \frac{2sb_6}{b_7} + 1\right)}{\left(\frac{s}{1000} + 1\right)^2}$$

The fixed poles were numerically set to 1000 radians per second to obtain a realizable structure. If the poles were not fixed, the search tended to drive the poles toward infinity with only a minimal improvement in control.

It is interesting to note that passive accumulators could be sized using this program. This is true so long as the device senses local pressures and modifies local flow and the defining equations are linear. The derivative controller could be considered a passive compliant accumulator because the defining equations are essentially the same.

CONTROLLER DESIGN

Performance Comparisons

Controllers were designed for each of the four structures presented in the previous section. The designs are for the case of no measurement noise. The weighting variable

r was changed to achieve different control efforts and performance. The resulting controller designs are compared in figure 4 on the basis of the design variables $\overline{P_7^2}$ and $\overline{Q_a^2}$ averaged square values. Each point on a curve corresponds to a parameter optimization for a particular value of the weighting variable r. The values of the design variables are reported as normalized values. The normalization of the pressure error P_7 was by the reference value obtained by integrating the square of the open-loop frequency response magnitude. The control level Q_a was normalized by using the level obtained from the derivative control structure with $b_2 = 80$; that is,

$$\left(\overline{P_7^2}\right)_N \equiv \frac{\overline{|P_7|^2}}{\overline{|P_7|^2}_{ref.}}$$

and

$$\left(\overline{Q_a^2}\right)_N \equiv \frac{\overline{|Q_a|^2}}{\overline{|Q_a|^2}_{ref.}}$$

where

$$\overline{|P_7|^2}_{ref.} = 1.5 \left[\frac{\left(\frac{N}{cm^2}\right)}{\left(\frac{cm^2}{sec \cdot rad}\right)}\right]^2 D\left(\frac{cm^3}{sec \cdot rad}\right)^2$$

$$= 3.2 \left[\frac{\left(\frac{lbf}{in.^2}\right)}{\left(\frac{in.^3}{sec \cdot rad}\right)}\right]^2 D\left(\frac{in.^3}{sec \cdot rad}\right)^2$$

and

$$\overline{|Q_a|^2}_{ref.} = 200\,000\, D\left(\frac{cm^3}{sec \cdot rad}\right)^2$$

$$= 710\, D\left(\frac{in.^3}{sec \cdot rad}\right)^2$$

The four controller structure curves (fig. 4) all show a decrease in pressure variation with an increase in control level (decreased r weighting). The first- and second-order lead-lag controllers reduce the pressure error more than the proportional controller over the range of control effort. Except for the case of proportional control, the pressure error is driven to vanishingly small values with increasing control effort. The derivative and lead-lag controller designs develop an almost vertical slope. (The proportional design also dropped, but at a greater control effort than shown in fig. 4.) The sharp drop indicates that very large controller gains reduce the pressure error to very small values without driving the system unstable. Use of such high gains would probably not be permitted if the suppressor actuator was more accurately modeled with a higher order transfer function and saturation limits were considered.

The curve for the derivative control appears as a shorter and more vertical line. The derivative control required about 84 percent of unity normalized control effort (and a minimum b_2 gain of about 0.65) to achieve system stability. It was the plant mode at about 2.3 hertz that made the system unstable for lower derivative gains. The proportional control was able to achieve a stable system with only about a fourth of the unity normalized control effort. For the proportional control case the plant mode at about 24 hertz was the limiting factor.

The lead-lag controllers were able to achieve stability with minimum control level. System stability for these controllers was achieved with less than about 5 percent of unity normalized control effort. The reduced effort is of course reflected back into the hydraulic flow requirements associated with a given controller design.

Controller Parameters

The values of the b parameters for the different h(s,b) control structures are tabulated in table II for 10-percent increments in control effort. The increase in control effort is closely related to increased controller gains. Between the 90 and 100 percent of unity control levels there is a sharp increase in the controller b_3 and b_5 gains (for the lead-lag and second-order lead-lag controllers). This occurs at the control effort levels at which the pressure variation almost vanishes (fig. 4). In the vicinity of this rapid change, the most interesting controllers can be chosen. Further analysis will be directed to the 90 and 100 percent of unity normalized control effort conditions.

Effects of Measurement Noise

The controller designs were obtained with no measurement noise. These controller designs were then evaluated for the case of measurement noise to obtain the noise

sensitivity of the controllers (fig. 5).

The D/V disturbance to noise ratio of psd values was set at 3.316×10^6 $[(cm^3/sec \cdot rad)/(N/cm^2 \cdot rad)]^2$ or 5870 $[(in.^3/sec \cdot rad)/(lbf/in.^2 \cdot rad)]^2$. This resulted in a pressure error $\overline{|P_7|_d^2}/\overline{|P_7|_v^2}$ ratio of 0.27 for the 90 percent of unity control effort lead-lag controller design, a rather harsh condition. At this noise level the control effort was increased 25 percent at the normalization point due to the noise. For comparison, the control effort values from figure 4 for the case of no measurement noise are listed beside each data point in figure 5. With measurement noise the pressure error does not drop to vanishingly small values. Both the pressure error created by the controller in attempting to control the noise $\overline{|P_7|_v^2}$ and the noise induced control effort $\overline{|Q_a|_v^2}$ increase with higher gain controllers. A more detailed design would consider different noise levels and optimize the controllers for the noise.

System Frequency Response

The frequency response of the system indicates how the cost function averages were obtained by giving an "unaveraged" view of the controller performance as a function of frequency. The frequency response of the P_7/d pressure variation to disturbance relationship is considered first. The frequency response magnitude $|P_7(j\omega)/d$ is plotted in figure 6(a) for the 90 percent of unity control effort designs. The open-loop response (from fig. 3(a)) is plotted again for comparison purposes. The proportional control forces the system above the open-loop response at the higher frequencies. The derivative control is above the proportional at low frequencies. The lead-lag and second-order lead-lag controllers show improvement in performance over the entire frequency range. The open- and closed-loop curves must all eventually coincide, but this occurs above the frequency range considered here.

Figure 6(b) is a similar plot of $|P_7(j\omega)/d|$ but for the higher gain unity control efforts designs. The derivative controller now has more attenuation at the lower frequencies. The attenuation of all the controllers is generally greater than the figure 6(a) levels. This is consistent with the increased control effort.

The frequency response magnitude of the suppressor flow to disturbance flow $|Q_a(j\omega)/d|$ relationship is considered next. These responses are plotted in figure 7 for the controller designs with 90 and 100 percent of unity control effort. The responses are generally flat showing the control effort is about equally effective over the frequency range. Variations in magnitude from the nominal level tend to indicate deviations from an ideal control.

System Eigenvalues

A study of the system closed-loop eigenvalues, which are the roots of the system characteristic equation $1 + G(s) = 0$, is made next. The system's two worst eigenvalue damping ratios were generally associated with the 2.3- and 24-hertz structural modes. The 2.3-hertz mode is considered first. The damping ratio for that mode is plotted versus control effort in figure 8(a). Damping decreases with decreased control for all designs, but the derivative curve falls off considerably faster. The 24-hertz mode is considered next (fig. 8(b)). Here, derivative action is relatively more effective for the 24-hertz mode than it was for the 2.3-hertz mode.

To illustrate the effect on the other modes, all the system structural mode eigenvalues are plotted in figure 9 for a specific controller, namely, the first-order lead-lag 90 percent of unity normalized control effort design. With this control, the damping ratios are all increased except for that mode associated with the 26.8-hertz structural mode. The discrete points are connected by lines for illustration only.

Sensitivity to Structural Frequency

It is of interest to examine system behavior for changes in the shuttle model. The change considered is the variation of the natural frequencies of structural modes.

The effect on the closed-loop damping for variations of the 24-hertz structural mode is considered first. This mode had about the lowest damping of all modes both with and without control. The performance using the 90 percent of unity control designs is considered first (fig. 10(a)). The open-loop damping is also plotted for comparison. Judging from the curves, the choice of a nominal frequency of 24 hertz for the worst-case condition was about right. The system is somewhat sensitive to plant changes. The more complex controllers do not always achieve the best damping. But all the controllers maintained system stability.

The stability of the unity normalized control level designs are considered next in figure 10(b). The derivative and second-order lead-lag results were nearly identical for this mode. The increase in control effort has not noticeably improved the system stability. To show this more clearly, the unity control lead-lag design (from fig. 10(b)) is compared with the corresponding 90 percent of unity design (from fig. 10(a)) in figure 11. The lower control level design has about the same average level of stability for this mode.

The sensitivity of the system to changes in the nominal 2.3-hertz structural mode is shown in figure 12 for controller designs with the 90 percent of unity control design. Here, the derivative controller can not maintain system stability for a decrease in natural frequency of about 2.3 hertz; whereas, the proportional and lead-lag designs show

good stability and little sensitivity to the plant changes. The unity control designs (not shown) showed little sensitivity to shifts in the nominal 2.3-hertz structural mode.

CONCLUSIONS

A frequency-domain parameter optimization technique is used in a preliminary design study of controllers for active pogo suppression control of the space shuttle. The design approach is considered a viable tool for pogo controller design studies. The technique is based on minimizing a cost function using a conjugate gradient search procedure. The cost function formulated consists of the averaged square variation of the controlled variable, the high-pressure oxidizer pump suction pressure P_7, and a weighted averaged square control. The space shuttle model was a two-pump, six-structural-mode linear state variable matrix model. The model represented a worst-case condition that was open-loop unstable.

The controller design proceeded by designing a series of controllers with increasingly complex structures. The four controller designs presented were proportional, derivative, lead-lag, and second-order lead-lag. The cost function averaged square values showed the design compromises between controller complexity and level of control effort. The supporting design studies included the effects of measurement noise, the frequency responses of the system, system eigenvalue damping ratios, and system sensitivity to changes in structural mode frequencies.

The system performance with the worst-case model improved for both an increase in controller complexity and control effort. Increased control effort was generally related to increased controller gains. The two lowest damping ratios increased uniformly with increased control. A sensitivity analysis of structural mode natural frequency showed that, except in the immediate vicinity of the design point, the damping did not necessarily uniformly improve with either increased control effort or increased filter complexity. The sensitivity analysis appears useful in the design approach to help select a suitable controller.

The lead-lag controller was a promising structure; its combination of proportional plus approximate derivative action achieved good control performance $\overline{P_7^2}$ with reasonable control effort. The lead-lag designs required the lowest levels of control to achieve system stability. They could attenuate the disturbance error over a broad range of

frequencies, and the designs were effective in increasing system damping for both the low- and high-frequency structural modes.

Lewis Research Center,
National Aeronautics and Space Administration,
Cleveland, Ohio, December 16, 1975,
505-05.

APPENDIX - SPACE SHUTTLE POGO MODEL

This appendix contains a description of the space shuttle oxidizer (liquid oxygen) system dynamic model used for this pogo controller design study. The model is basically the one described in references 3 and 4. It has been modified to meet the needs of this study as well as other studies conducted at Lewis. The model can be divided into a structural portion and a propulsion system portion. The structural model is a six-mode approximation describing the liquid oxygen (lox) feedline motion. This model is based on one developed by the Aerospace Corporation and uses structural model shape data presented in references 3 and 4. The propulsion system portion, modified at Lewis is a linear, lumped-parameter model of the lox feedlines, pumps, and thrust-chamber dynamics. The two portions of the model are joined through consideration of drag and momentum force coupling terms.

The differential equations that describe the combined structural-propulsion system model are presented. To obtain the transfer functions required in the pogo controller design study, these equations were put in state-variable form. Then the transfer functions were conveniently obtained using existing computer programs (ref. 5).

Symbols

A	cross sectional area, cm^2
a	acoustic velocity, m/sec
C	compliance, cm^5/N
C_{b1}	LPOP compliance, cm^5/N
C_{b2}	HPOP compliance, cm^5/N
c_f	discharge coefficient, dimensionless
F	force, N
$\mathscr{F}$	generalized force, N
$\bar{f}$	mean mass flow of lox, g/sec
g	gravitational constant, N/g
i	component of vector
j	component of vector
L	inertance, $N \cdot sec^2/cm^5$
l	line length, cm

$\ell 1$	vertical feedline segment
$\ell 2$	horizontal feedline segment
$m_1 + 1$	LPOP dynamic gain, dimensionless
$m_2 + 1$	HPOP dynamic gain, dimensionless
M	generalized mass, g
P	pressure, N/cm^2
$\mathscr{P}$	modal pressure coefficient, $N \cdot sec^2/cm^3$
P_7	HPOP suction pressure variation, N/cm^2
p	pressure in feedline lump, N/cm^2
Q	volumetric flow rate, cm^3/sec
q	generalized displacement, cm
$\overline{q}$	volumetric flow rate in feedline lump, cm^3/sec
R	resistance, $N\ sec/cm^5$
tb	tank base
x	structural displacement along vertical axis, cm
z	structural displacement along horizontal axis, cm
ζ	damping ratio
ρ	lox density, g/cm^3
τ_c	time constant, sec
ω	structural pole natural frequency, rad/sec
φ	modal displacement coefficient, dimensionless
ψ	mode shape vector, dimensionless

Subscripts:

a	actuator
b1	bubble for LPOP
b2	bubble for HPOP
c	thrust chamber
d	discharge line
d7	disturbance at station 7
I	inner pump duct

i index

J injector

j index

k index

ℓ lump

$\ell 1$ first (vertical) feedline

$\ell 2$ second (horizontal) feedline

n structural mode

p1 LPOP

p2 HPOP

tb tank base

Superscripts:

(x) x direction

(z) z direction

System Geometry

For dynamic modeling purposes a simplified lox feedline - pump-chamber geometry, developed by the Aerospace Corporation, was used (see fig. 13). The system consists of the lox tank connected to a 31.1-meter (102-ft) long, 0.25-meter (0.82-ft) diameter vertical feedline, an elbow, followed by a 8.47-meter (27.8-ft) long, 0.25-meter (0.82-ft) diameter horizontal feedline connected to the LPOP. A short interpump duct connects the LPOP with the HPOP, which pumps the lox through a discharge duct into the thrust chamber. The suppressor location is at the inlet to the HPOP.

The Aerospace structural model defines seven lox system structural elements that can move independently of one another. They are the lox tank, the two feedline segments, the two elbows, the LPOP, and the interpump-duct - HPOP - discharge-line - thrust-chamber combination. As indicated by the velocity coordinates shown in figure 13, the tank and the two feedlines can each move in only their axial directions ($\dot{x}_{tb}$, $\dot{x}_{\ell 1}$, and $\dot{z}_{\ell 2}$), but the elbows and pump assemblies are free to move both horizontally and vertically. Propulsion system dynamics are characterized by volumetric flow rates Q_i and pressures P_i throughout the system. The subscripts i correspond to station locations: tb, tank base; 1, first elbow; 2, entrance to horizontal feedline; 3, second elbow; 4, LPOP inlet; 5, LPOP exit; 7, HPOP inlet; c, thrust chamber. These station definitions are the same as those used in references 3 and 4.

Propulsion System Dynamic Equations

The propulsion system portion is modeled as a lumped parameter system. The vertical feedline is broken up into nine lumps and the horizontal feedline into three lumps. Figure 14 shows a typical lump, or control volume, used in obtaining the feedline equations. Shown is the i^{th} lump, occurring in the horizontal (second) feedline. The vertical feedline equations, considering conservation of mass and momentum for each lump, can be written as

$$\dot{\bar{q}}_1 = -\frac{R_l}{L_l}\bar{q}_1 - \frac{p_1}{L_l} + \frac{P_t}{L_l} - \frac{R_l A_1}{L_l}\dot{x}_{l1}$$

$$\dot{\bar{q}}_i = -\frac{R_l}{L_l}\bar{q}_i - \frac{p_i}{L_l} + \frac{p_{i-1}}{L_l} - \frac{R_l A_1}{L_l}\dot{x}_{l1} \qquad i = 2,3,\ldots,9$$

$$\bar{q}_9 \triangleq Q_1$$

$$\dot{p}_i = \frac{1}{C_l}(\bar{q}_i - \bar{q}_{i+1}) \qquad i = 1,2,\ldots,8$$

$$p_8 \triangleq P_1$$

$$\dot{p}_9 \triangleq \dot{P}_2 = \frac{1}{C_l}(Q_1 - Q_2 + A_1\dot{x}_1 + A_1\dot{z}_1)$$

Similarly, the following equations can be written for the horizontal feedline:

$$\dot{\bar{q}}_{10} \triangleq \dot{Q}_2 = -\frac{R_l}{L_l}\bar{q}_{10} - \frac{p_{10}}{L_l} + \frac{P_2}{L_l} + \frac{R_l A_2}{L_l}\dot{z}_{l2}$$

$$\dot{\bar{q}}_{11} = -\frac{R_l}{L_l}\bar{q}_{11} - \frac{p_{11}}{L_l} + \frac{p_{10}}{L_l} + \frac{R_l A_2}{L_l}\dot{z}_{l2}$$

$$\dot{\bar{q}}_{12} \triangleq \dot{Q}_4 = -\frac{R_l}{L_l}\bar{q}_{12} - \frac{p_{12}}{L_l} + \frac{p_{11}}{L_l} + \frac{R_l A_2}{L_l}\dot{z}_{l2}$$

$$\dot{p}_{10} = \frac{1}{C_l} (\bar{q}_{10} - \bar{q}_{11})$$

$$\dot{p}_{11} = \frac{1}{C_l} (\bar{q}_{11} - \bar{q}_{12})$$

The cross-sectional areas of the two lines are assumed equal ($A_1 = A_2 = A$), thus the compliance per lump is

$$C_l = \frac{gA\ell}{\rho a^2}$$

where g is the gravitational constant, ρ is the lox density, a is the speed of sound in lox, L_l $(=\rho\ell/Ag)$ is the inertance per lump, R_l is the resistance per lump, and P_{tb} is the tank base pressure.

The equation for the pressure at the inlet to the LPOP can be written considering the cavitation bubble compliance, the motion of the elbow (3), and LPOP (4) as they affect the fluid system. The result is

$$\dot{p}_{12} \triangleq \dot{P}_4 = \frac{1}{C_{b1}} (Q_4 - Q_5) + \frac{A_2}{C_{b1}} (\dot{x}_4 - \dot{x}_3) + \frac{A_3}{C_{b1}} \dot{z}_4 - \frac{A_2}{C_{b1}} \dot{z}_3$$

where C_{b1} is the cavitation bubble compliance and A_3 is the LPOP exit area, which equals the interpump duct area. The equations for the interpump duct were written considering the duct as one lump with resistance R_I, inertance L_I, and cavitation compliance C_{b2} at the HPOP inlet. The resulting equations are

$$\dot{Q}_5 = \frac{1}{L_I + L_{p1}} \left[(m_1 + 1)P_4 - P_7 - (R_I + R_{p1})Q_5 + R_{p1}A_3\dot{z}_4 + R_I A_3 \dot{z}_7\right]$$

$$P_5 = (m_1 + 1)P_4 - R_{p1}Q_5 - L_{p1}\dot{Q}_5 + R_{p1}A_3\dot{z}_4$$

$$\dot{P}_7 = \frac{1}{C_{b1}} \left[Q_5 - Q_c + Q_a + Q_{d7} + (A_4 - A_3)\dot{z}_7\right]$$

where L_{p1} is the LPOP inertance, $m_1 + 1$ is the LPOP gain, R_{p1} is the LPOP resistance, Q_a is the suppressor flow rate (located at the HPOP inlet), Q_{d7} is the flow disturbance occurring at the HPOP inlet, and A_4 is the HPOP suction area. All parameters associated with the pumps and interpump duct were obtained from references 3

and 4. Completing the propulsion system model, the equations for the discharge line and thrust chamber pressure P_c and flow Q_c can be written as

$$\dot{Q}_c = \frac{1}{L_d + L_J + L_{p2}} \left[P_7 - P_c - (R_d + R_J + R_{p2})Q_c + A_4\dot{z}_7\right]$$

and

$$P_c = \frac{R_c}{\tau_c}\left(Q_c - \frac{P_c}{R_c} - A_4\dot{z}_7\right)$$

where the following parameters were also obtained from references 3 and 4: L_d is the discharge line inertance, L_J is the injector inertance, L_{p2} is the HPOP inertance, R_d is the discharge line resistance, R_J is the injector resistance, R_{p2} is the HPOP resistance, R_c is the thrust chamber resistance, and τ_c is the thrust chamber time constant.

Structural Dynamic Equations

As indicated previously, the structural model used is based on that of references 3 and 4. In the model seven structural elements are identified that characterize the lox system. Primary structural output quantities of interest are the horizontal $\dot{z}$ and vertical $\dot{x}$ velocities of each element. The structural elements and their associated indexes are tb, tank base; $\ell 1$, vertical feedline; 1, first elbow; $\ell 2$, horizontal feedline; 3, second elbow; 4, LPOP; 7, interpump duct-HPOP-discharge line-thrust chamber combination.

The structural model was developed as was done in references 3 and 4 except for the treatment of feedline drag forces. The modal equations can be written as

$$M_n\left(\ddot{q}_n + 2\zeta_n\omega_n\dot{q}_n + \omega_n^2 q_n\right) = \mathcal{F}_n \qquad n = 1, 2, \ldots, 6$$

where M_n is the generalized mass of the n^{th} mode, q_n is the generalized displacement of the n^{th} mode, ζ_n is the n^{th} mode damping ratio, ω_n is the n^{th} mode natural frequency, and $\mathcal{F}_n$ is the generalized force associated with the n^{th} mode.

The model in references 3 and 4 has six modes, which are assumed to adequately describe the system at a particular flight condition. In this model the structural velocities $\dot{x}_i$ and $\dot{z}_i$ can be related to the six generalized velocities $\dot{q}_n$ by

$$\dot{x}_i = \sum_{n=1}^{6} \varphi_n^{(x)}(i)\dot{q}_n; \qquad i = \ell 1, 1, 3, 4, 7, tb$$

$$\dot{z}_i = \sum_{n=1}^{5} \varphi_n^{(z)}(i)\dot{q}_n; \qquad i = \ell 2, 1, 3, 4, 7$$

where $\varphi_n^{(x)}(i)$ and $\varphi_n^{(z)}(i)$ are components of the mode shape vectors. For example, the n^{th} mode shape vector ψ_n is written as

$$\psi_n = \begin{bmatrix} \varphi_n^{(x)}(\ell 1) \\ \varphi_n^{(x)}(1) \\ \varphi_n^{(x)}(3) \\ \varphi_n^{(x)}(4) \\ \varphi_n^{(x)}(7) \\ \varphi_n^{(x)}(tb) \\ \varphi_n^{(z)}(\ell 2) \\ \varphi_n^{(z)}(1) \\ \varphi_n^{(z)}(3) \\ \varphi_n^{(z)}(4) \\ \varphi_n^{(z)}(7) \end{bmatrix}$$

where the ordering of structural velocities is arbitrary. The remaining structural output, tank pressure, can be related to the generalized accelerations, as shown in references 3 and 4, as

$$P_{tb} = \sum_{i=1}^{6} \mathscr{P}_i(tb)\ddot{\bar{q}}_i$$

where coefficients $\mathscr{P}_i(tb)$ are given.

The generalized force on the n^{th} mode was shown in references 3 and 4 to be

$$\mathscr{F}_n = \mathscr{P}_n(tb)\left[\dot{\bar{q}}_1 + A_1\sum_{k=1}^{6}\bar{q}_k\varphi_k^{(x)}(tb)\right] + P_{tb}A_1\varphi_n^{(x)}(tb) + \sum_i F_i^{(x)}\varphi_n^{(x)}(i) + \sum_j F_j^{(z)}\varphi_n^{(z)}(j)$$

where

$i = \ell 1, 1, 3, 4, 7, tb$

$j = \ell 2, 1, 3, 4, 7$

$n = 1, 2, \ldots, 6$

The first term accounts for forces generated by lox tank out-flow and the second for forces due to tank pressure variation. The terms $F_i^{(x)}$ and $F_j^{(z)}$ are the actual forces on the structure due to flow rate, pressure, and structural velocities at the seven defined locations. These forces are made up of (1) drag forces on the feedlines, interpump duct, and discharge line, (2) momentum forces at the two feedline corners, the LPOP, and the HPOP, and (3) forces on the thrust chamber.

In a manner similar to that used in references 3 and 4, these forces can be expressed as follows in terms of structural velocities and flows and pressures previously defined.

Vertical and horizontal feedlines: The modeling here differs from that used in references 3 and 4 since the feedline models are lumped instead of distributed. The drag forces are

$$F_{\ell 1}^{(x)} = -A_1 R_\ell\left(\sum_{i=1}^{9}\bar{q}_i + A_1\dot{x}_{\ell 1}\right)$$

$$F_{\ell 2}^{(z)} = A_2 R_\ell\left(\sum_{i=10}^{12}\bar{q}_i - A_2\dot{z}_{\ell 2}\right)$$

First elbow:

$$F_1^{(x)} = -P_2A_1 - \bar{f}\left(2\frac{Q_1}{A_1} + \dot{x}_1\right)$$

$$F_1^{(z)} = -P_2A_2 - \bar{f}\left(2\frac{Q_2}{A_2} - \dot{z}_1\right)$$

Second elbow:

$$F_z^{(x)} = P_4A_2 + \bar{f}\left(2\frac{Q_4}{A_2} + \dot{x}_3\right)$$

$$F_3^{(z)} = P_4A_2 + \bar{f}\left(2\frac{Q_4}{A_2} + \dot{z}_3 + 2\dot{x}_3\right)$$

LPOP:

$$F_4^{(x)} = -P_4A_2 - \bar{f}\left(2\frac{Q_4}{A_2} + \dot{x}_4\right)$$

$$F_4^{(z)} = -P_5A_3 - \bar{f}\left(2\frac{Q_5}{A_3} - \dot{z}_4\right)$$

Interpump-duct - HPOP-discharge line-thrust chamber:

$$F_7^{(x)} = A_c c_f P_c$$

$$F_7^{(z)} = A_3R_I(Q_7 - A_3\dot{z}_7) + A_4R_d(Q_c - A_4\dot{z}_7) + P_7A_3 - P_cA_4 + 2\bar{f}\left(\frac{Q_7}{A_3} - \frac{Q_c}{A_4}\right) + A_4P_c$$

Here, $\bar{f}$ is the mean mass flow of the lox, A_c is the thrust chamber area, and c_f is the discharge coefficient.

Parameter Values

The nominal parameters that characterize the propulsion system are given in table III. All, except for line inertance and compliance and for actuator frequency, are obtained from references 3 and 4.

Bubble compliances C_{b1} and C_{b2} and pump gains $m_1 + 1$ and $m_2 + 1$ are especially dependent on flight condition. The values shown in table III define the expected parameter ranges. Structural parameters required are mainly the modal vector data, plus modal frequencies, masses, and damping ratios. Table IV presents these data, which are adapted from data in references 3 and 4, for the two flight conditions of interest - end burn and after solid rocket separation. These two conditions were chosen because preliminary analysis showed their pogo instabilities to be most pronounced.

Nominal Worst-Case Model

A nominal worst-case model was developed to reflect the dynamics of the two most critical flight conditions, end burn and after solid rocket separation, and to achieve an open-loop model of the more unstable condition. The worst-case model is basically the reference 3 model at end burn except for the following: The end burn structural mode at 2.81 hertz (E1) was replaced by a less stable mode (A1) from the after separation condition (see table IV). The frequency of the fifth end burn mode was shifted from 26.8 hertz to 24 hertz making the system open-loop unstable. Also, the LPOP and HPOP gains were set to the maximum expected values shown in table III, and the pump inlet bubble compliances were set to the minimum values shown in table III.

REFERENCES

1. Farrell, E. C.; and Fenwick, J. R.: Pogo Instabilities Suppression Evaluation. (R-9125, Rockwell Interal. Corp.; NA3-14382) NASA CR-134500, 1973.

2. Seidel, Robert C.; and Lehtinen, Bruce: Control System Design Using Frequency Domain Models and Parameter Optimization, with Application to Supersonic Inlet Controls. NASA TM X-3108, 1974.

3. Lock, M. H.; and Rubin, S.: Active Suppression of Pogo on the Space Shuttle. (ATR-75(7428)-1, Aerospace Corp.; NAS3-17758) NASA CR-134749, 1974.

4. Lock, M. H.; and Rubin, S.: Passive Suppression of Pogo on the Space Shuttle. (ATR-74(7416)-1; Aerospace Corp.; NAS1-12215) NASA CR-132452, 1974.

5. Seidel, Robert C.: Computer Programs for Calculation of Matrix Stability and Frequency Response from a State-Space System Description. NASA TM X-71581, 1974.

TABLE I. - DAMPING RATIOS AND NATURAL FREQUENCIES

OF OPEN-LOOP PLANT G(s) COMPLEX ROOTS

Damping ratio	Natural frequency, Hz	Damping ratio	Natural frequency, Hz
0.000784	[a]2.31	0.0190	[a]26.30
.165	2.89	.0180	28.11
.00986	[a]4.72	.0190	32.99
.00476	[a]8.38	.0130	35.91
.267	8.91	.00750	39.30
.0449	14.10	.00441	42.26
.0412	19.42	.00261	44.63
.00898	[a]22.50	.00162	46.36
.122	23.30	.00110	47.41
-.00151	[a]23.83		

[a]Compare with uncoupled structural mode natural frequencies of 2.30, 4.73, 8.49, 22.50, 24.00, and 26.80 Hz, respectively.

TABLE II. - CONTROLLER PARAMETERS FOR DIFFERENT

CONTROL EFFORT DESIGNS

Control effort, $(\bar{Q}_a^2)_n$, percent of unity	Controller structure and parameters						
	Proportional gain, b_1	Derivative gain, b_2	Lead-lag		Second-order lead-lag		
			Gain, b_3	Zero, b_4, rad/sec	Gain, b_5	Damping ratio, b_6	Zero natural frequency, b_7, rad/sec
10	----	---	4.8	108	6	0.43	237
20	(a)	---	8.5	128	13	.68	258
30	20.2	---	12.0	122	22	.52	257
40	25.2	---	14.5	109	32	.48	251
50	30.2	---	17.0	97	46	.44	245
60	35.2	---	20.2	87	67	.42	240
70	40.2	---	25.0	75	100	.40	236
80	45.3	(a)	35	62	160	.395	232
90	50.5	1	50	51	370	.385	228
100	55.7	80	200	46	7000	.380	224

[a]System unstable due to controller gain being below lower limit for stability.

TABLE III. - PROPULSION SYSTEM PARAMETERS

A_1	First feedline cross sectional area, cm^2; $in.^2$	487; 75.5
A_2	Second feedline cross sectional area, cm^2; $in.^2$	487; 75.5
A_3	LPOP exit area, cm^2; $in.^2$	201; 31.2
A_4	HPOP suction area, cm^2; $in.^2$	83.3; 12.6
$A_c c_f$	Effective thrust chamber area, cm^2; $in.^2$	1020; 158
a	Acoustic velocity a, m/sec; in./sec	5.183; 20 400
C_l	Lump compliance, cm^5/N; $in.^5/lbf$	5.94; 0.250
C_{b1}	HPOP compliance, cm^5/N; in./lbf	5.94 - 23.8; 0.25 - 1
C_{b2}	LPOP compliance, cm^5/N; in./lbf	2.38 - 2.98; 0.1 - 0.125
$\bar{f}$	Mean flow of liquid oxygen, N·sec/cm; lbf·sec/in.	4.01; 2.29
g	Gravitational constant, cm/sec^2; in./sec	981.5; 386.4
l	Line length, cm; in.	345; 136
L_l	Lump inertance, $N \cdot sec^2/cm$; $lbf \cdot sec^2/in.^5$	7.46×10^{-6}; 1.77×10^{-4}
L_I	Inner pump duct inertance, $N \cdot sec^2/cm$; $lbf \cdot sec^2/in.^5$	2.25×10^{-5}; 5.36×10^{-4}
L_{p1}	LPOP inertance, $N \cdot sec^2/cm$; $lbf \cdot sec^2/in.^5$	1.73×10^{-6}; 4.12×10^{-5}
L_{p2}	HPOP inertance, $N \cdot sec^2/cm$; $lbf \cdot sec/in.^5$	4.33×10^{-6}; 1.03×10^{-4}
L_d	Discharge line inertance, $N \cdot sec^2/cm$; $lbf \cdot sec/in.^5$	2.60×10^{-5}; 6.18×10^{-4}
L_J	Injector inertance, $N \cdot sec^2/cm$; $lbf \cdot sec/in.^5$	8.67×10^{-6}; 2.06×10^{-4}
$m_1 + 1$	LPOP gain	1.31 - 2.20
$m_2 + 1$	HPOP gain	1.42 - 1.54
R_l	Lump resistance, $N \cdot sec/cm^5$; $lbf \cdot sec/in.^5$	4.14×10^{-6}; 9.85×10^{-5}
R_I	Inner pump duct resistance, $N \cdot sec/cm^5$; $lbf \cdot sec/in.^5$	1.91×10^{-4}; 4.53×10^{-3}
R_{p2}	HPOP resistance, $N \cdot sec/cm^5$; $lbf \cdot sec/in.^5$	4.58×10^{-3}; 0.109
R_d	Discharge line resistance, $N \cdot sec/cm^5$; $lbf \cdot sec/in.^5$	8.49×10^{-4}; 2.029×10^{-2}
R_J	Injector resistance, $N \cdot sec/cm^5$; $lbf \cdot sec/in.^5$	6.17×10^{-3}; 0.147
R_c	Thrust chamber resistance, $N \cdot sec/cm^5$; $lbf \cdot sec/in.^5$	4.33×10^{-3}; 0.103
ρ	Liquid oxygen density, g/cm^3; lb/in.	1.055; 3.813×10^{-2}
τ_c	Thrust chamber time constant, sec	4.5×10^{-4}

TABLE IV. - STRUCTURAL MODE DATA FOR END BURN

AND AFTER SEPARATION CONDITIONS

Parameter		End burn						After separation
		Mode number, i						
		1	2	3	4	5	6	1
		Aerospace designation						
		E1	E2	E7	E30	E34	E35	A1
Modal displacement	$\varphi_i^{(x)}(\ell 1)$	-0.156	-0.198	0.054	0.022	0.222	0.022	0.529
	$\varphi_i^{(x)}(1)$	-0.330	-0.245	-0.0787	-0.752	0.370	0.0134	0.208
	$\varphi_i^{(x)}(3)$	-0.330	-0.245	-0.0787	-0.752	0.370	0.0134	0.208
	$\varphi_i^{(x)}(4)$	0.255	0.239	-0.556	-1.71	-2.13	2.63	1.28
	$\varphi_i^{(x)}(7)$	0.255	0.239	-0.556	-1.71	-2.13	2.63	1.28
	$\varphi_i^{(x)}(tb)$	-0.209	-0.334	-0.259	-7.74	4.443	5.336	0.257
	$\varphi_i^{(z)}(\ell 2)$	0.0367	-0.352	0.431	-0.372	0.017	-0.09	0.094
	$\varphi_i^{(z)}(1)$	0.0367	-0.352	0.431	-0.372	0.017	-0.09	0.094
	$\varphi_i^{(z)}(3)$	0.0367	-0.352	0.431	-0.372	0.017	-0.09	0.094
	$\varphi_i^{(z)}(4)$	0.846	0.50	-1.95	-0.12	0.99	-1.56	1.68
	$\varphi_i^{(z)}(7)$	0.846	0.50	-1.95	-0.12	0.99	-1.56	1.68
Modal pressure coefficient, $N \cdot sec^2/cm^3$	$\mathcal{P}_i(tb)$	0	0	0	0	0	0	-2.16×10^{-3}
Generalized mass	M_i	292	292	292	292	292	292	1282
Damping	ζ_i	0.01	0.01	0.01	0.01	0.01	0.01	0.01
Structural pole natural frequency, Hz	$2\pi\omega_i$	2.81	4.73	8.99	22.5	26.8	27.2	2.30

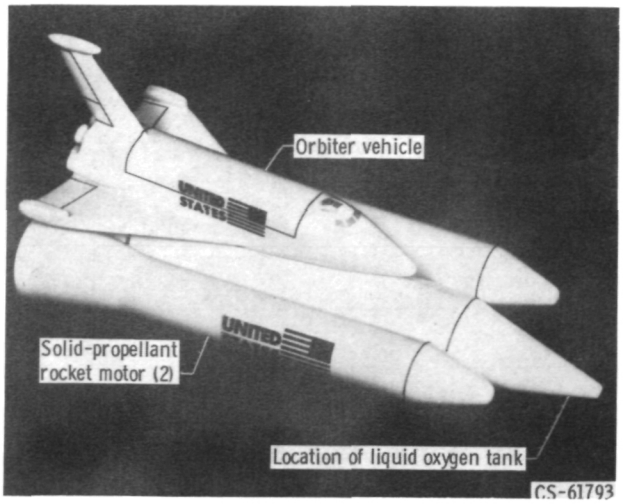

(a) Overall geometry.

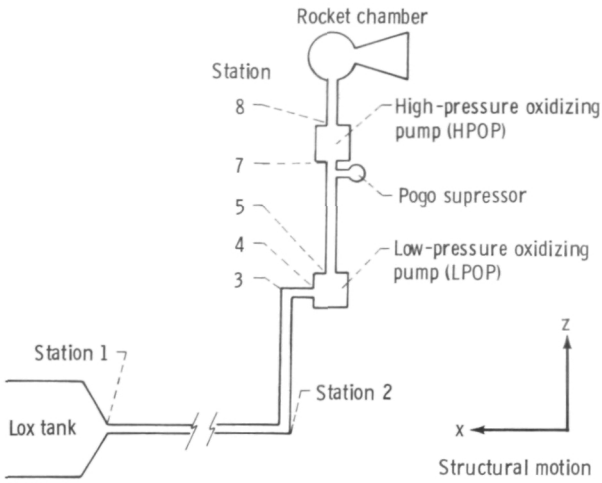

(b) Liquid oxygen (lox) system schematic.

Figure 1. - Shuttle system.

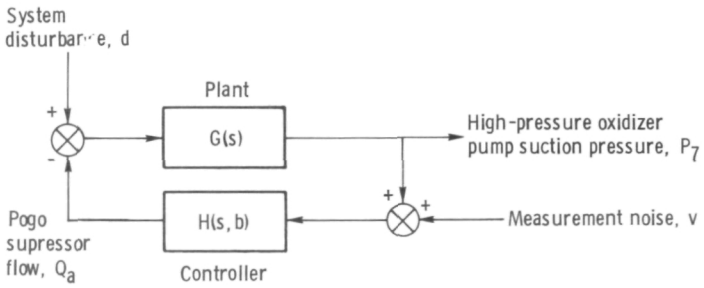

Figure 2. - System closed-loop block diagram for feedback controller.

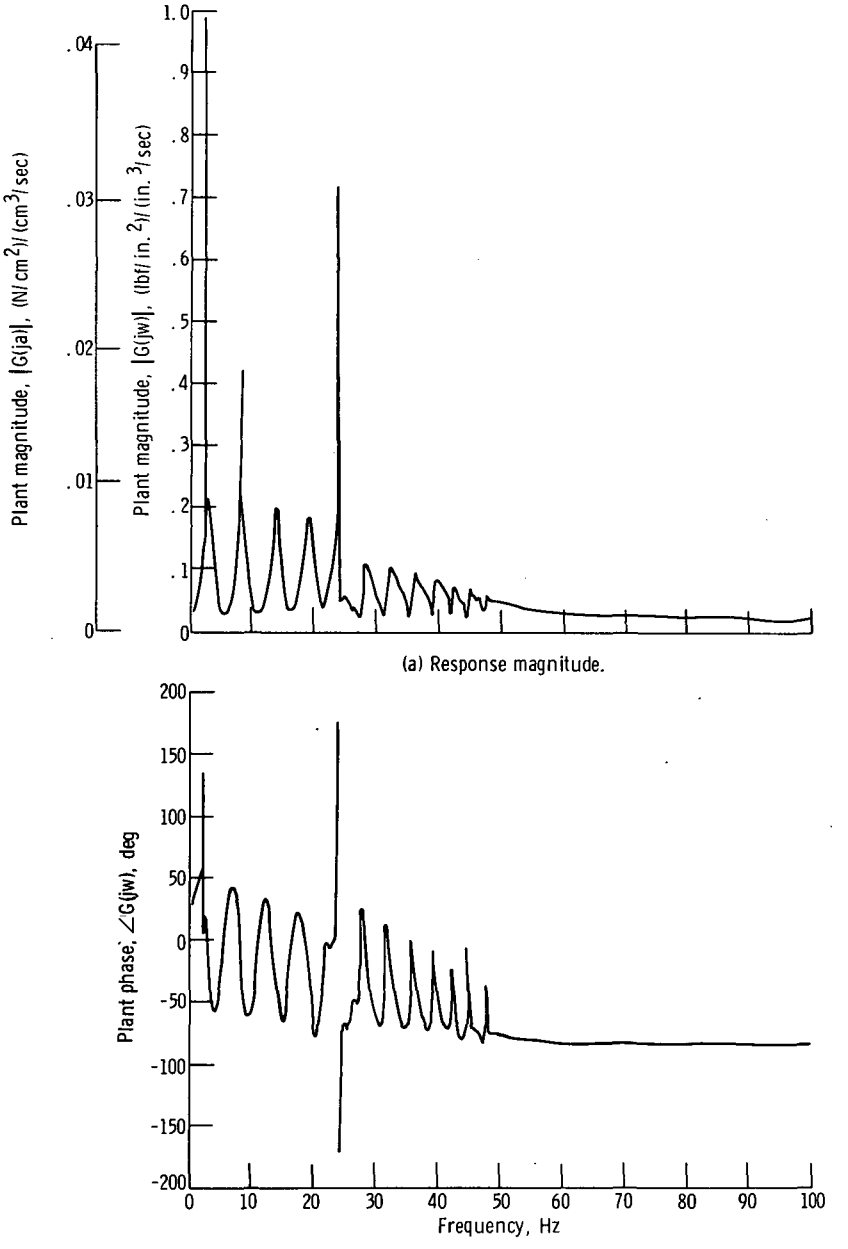

(a) Response magnitude.

(b) Response phase.

Figure 3. - Plant transfer function $G(jw) = P_7(j\omega)$/d open-loop frequency response.

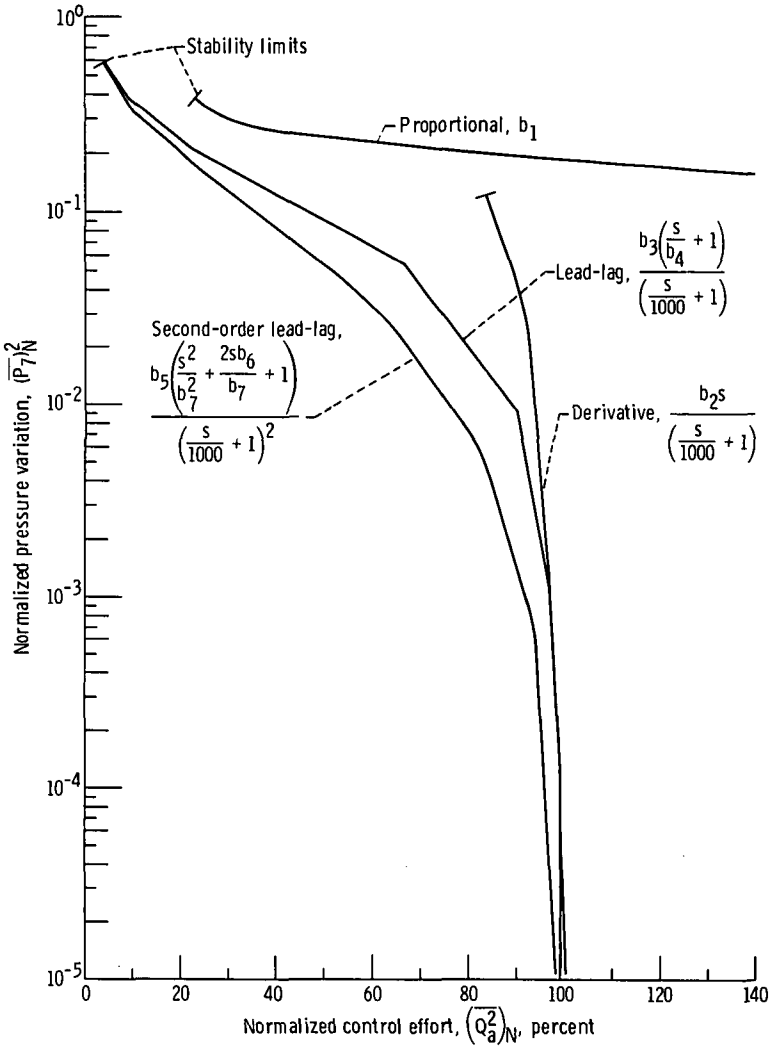

Figure 4. - Normalized controller performance averaged square pressure variation versus level of control effort for different controller structures designed for no measurement noise.

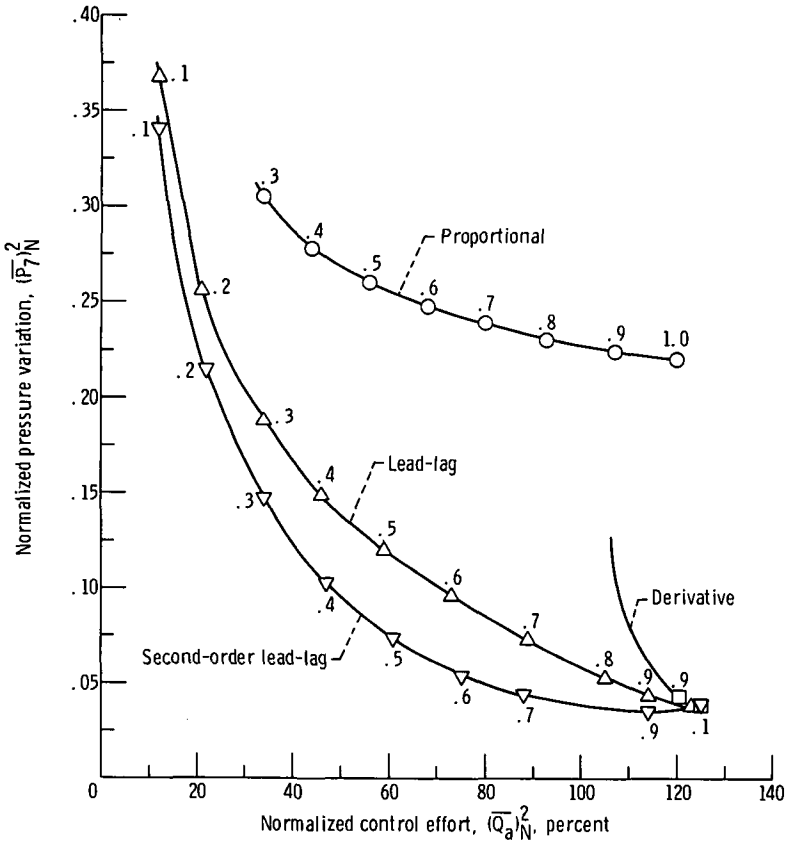

Figure 5. - Normalized controller performance averaged square pressure variation versus level of control effort with measurement noise. (Data point values denote normalized control levels for case of no measurement noise.)

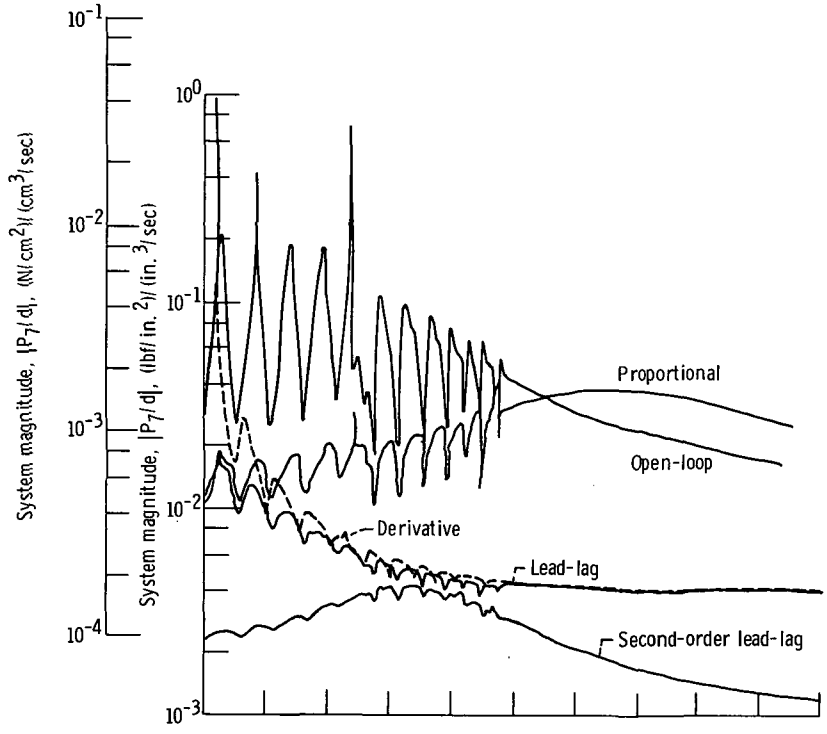

(a) Controller designs for 90 percent normalized control effort.

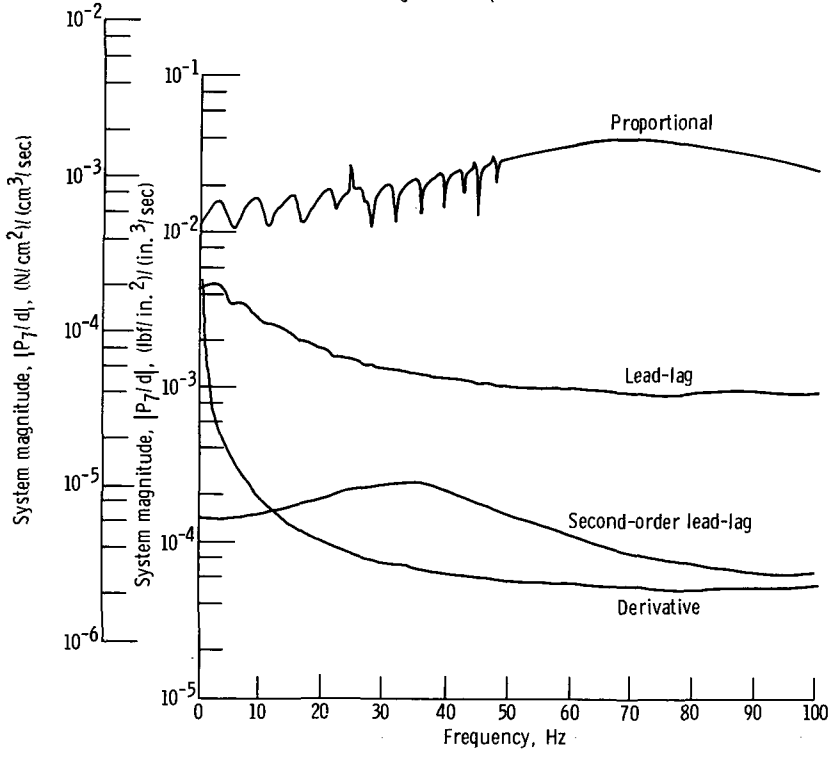

(b) Controller designs for 100 percent normalized control effort.

Figure 6. - Frequency response magnitude of pressure variation $P_7(j\omega)$ to disturbance d.

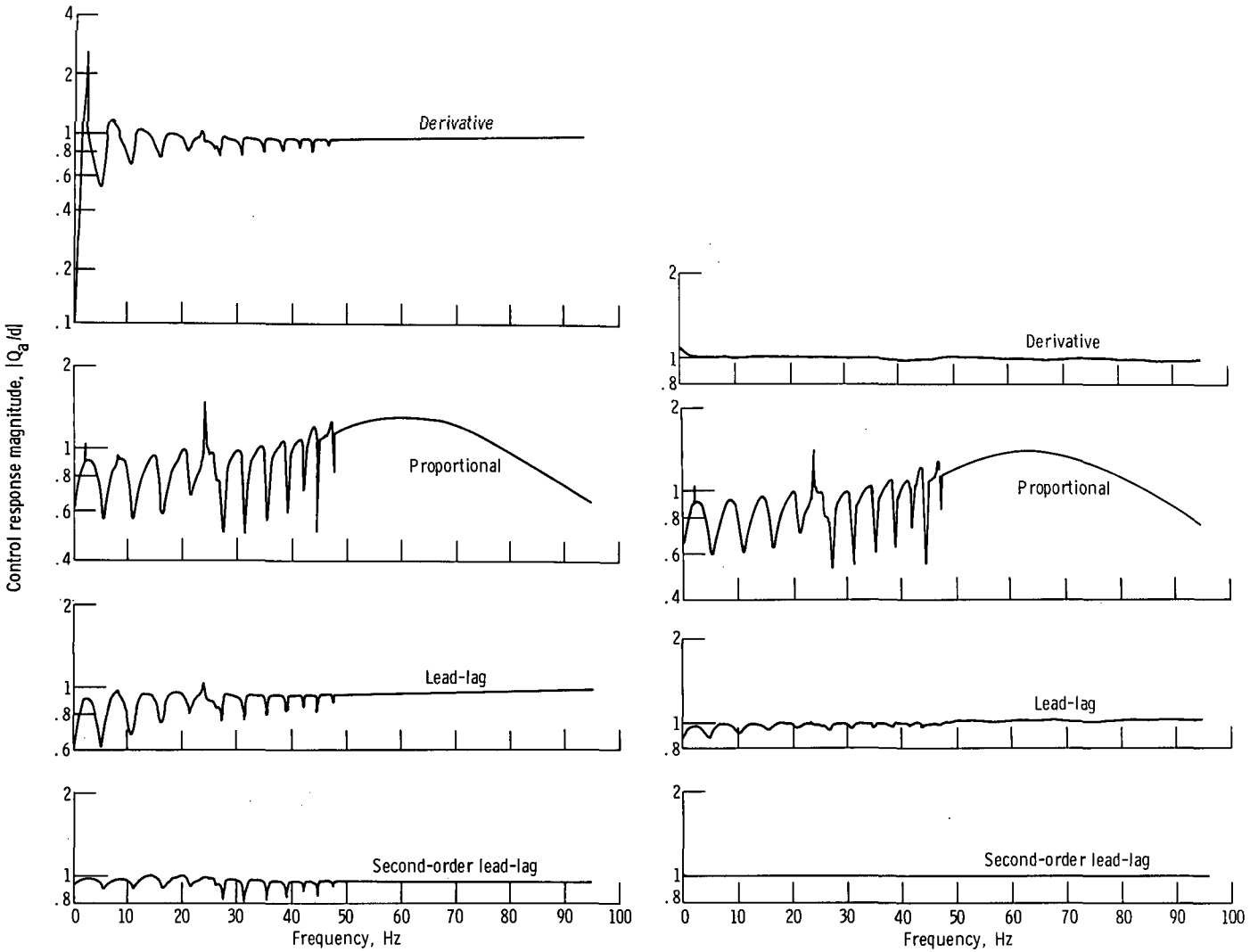

(a) Controller designs for 90 percent normalized control effort.

(b) Controller designs for 100 percent normalized control effort.

Figure 7. - Frequency response magnitude of suppressor flow Q_a to feedline disturbance flow d.

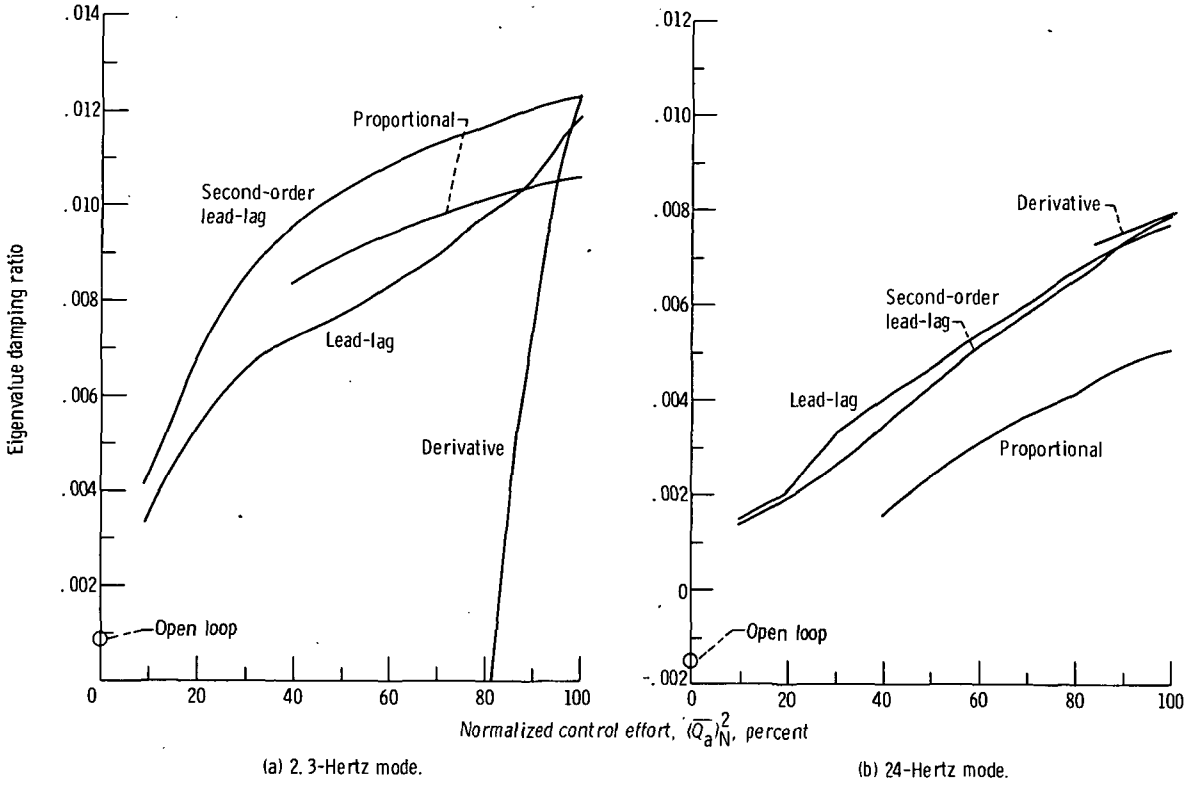

(a) 2.3-Hertz mode. (b) 24-Hertz mode.

Figure 8. - System eigenvalue damping ratio of structural mode versus control level for four controllers.

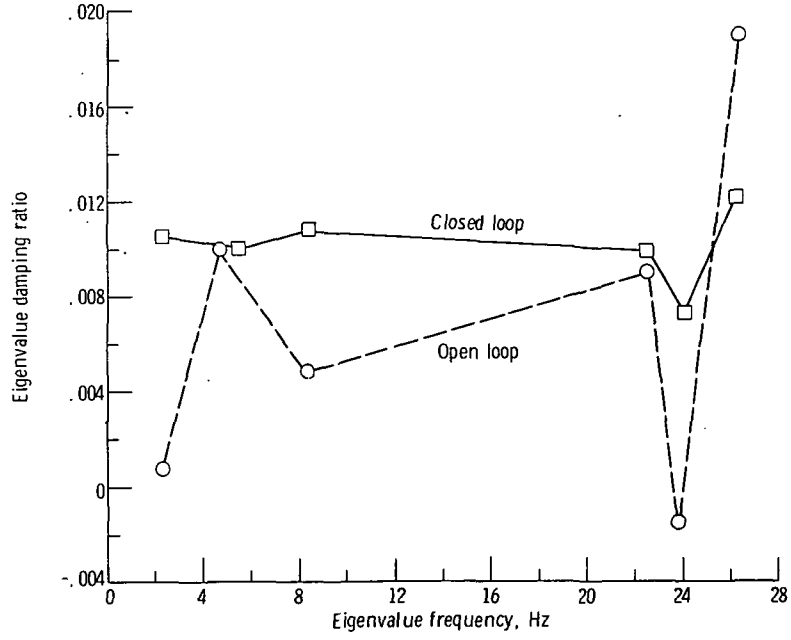

Figure 9. - Comparison of closed-loop and open-loop structural mode eigenvalue damping ratios. Lead-lag controller; 90 percent of unity normalized control level.

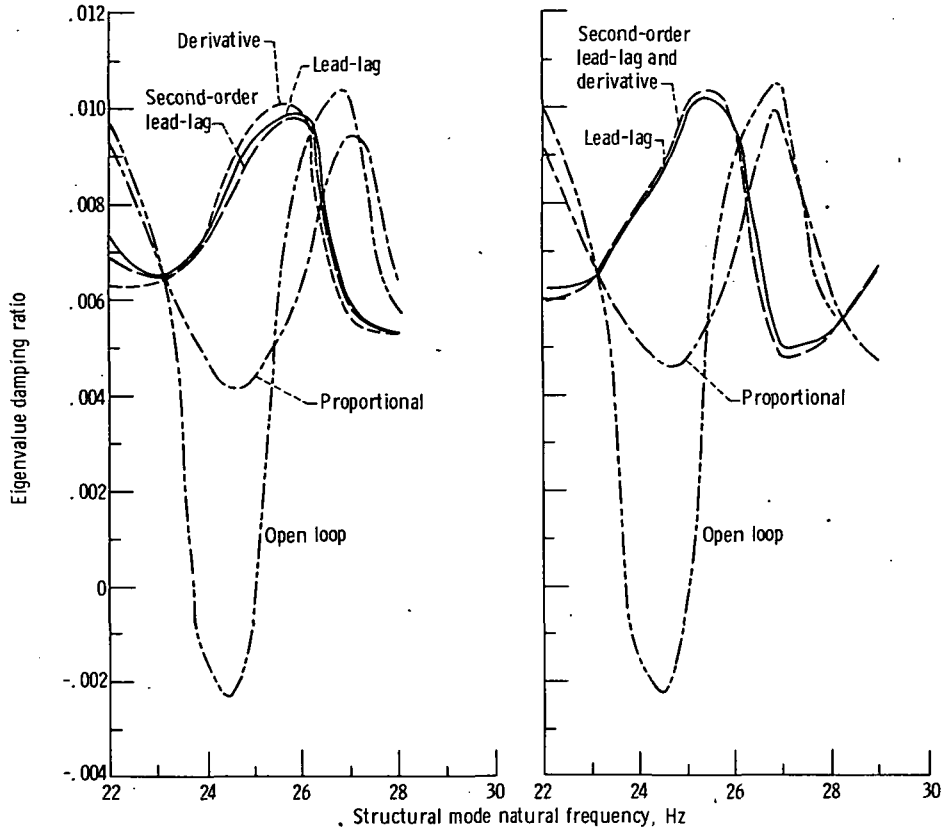

(a) 90 Percent of unity normalized control level. (b) Unity normalized control effort.

Figure 10. - Sensitivity of eigenvalue damping ratio to variations in 24-hertz structural mode frequency.

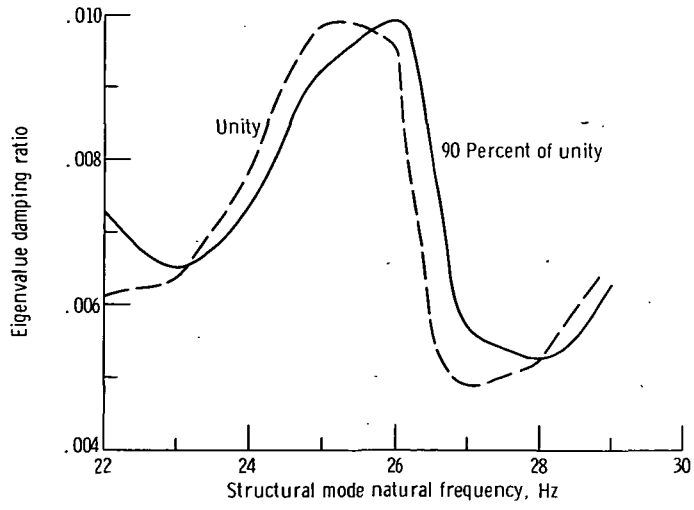

Figure 11. - Sensitivity comparison of lead-lag controller structure with two normalized control levels.

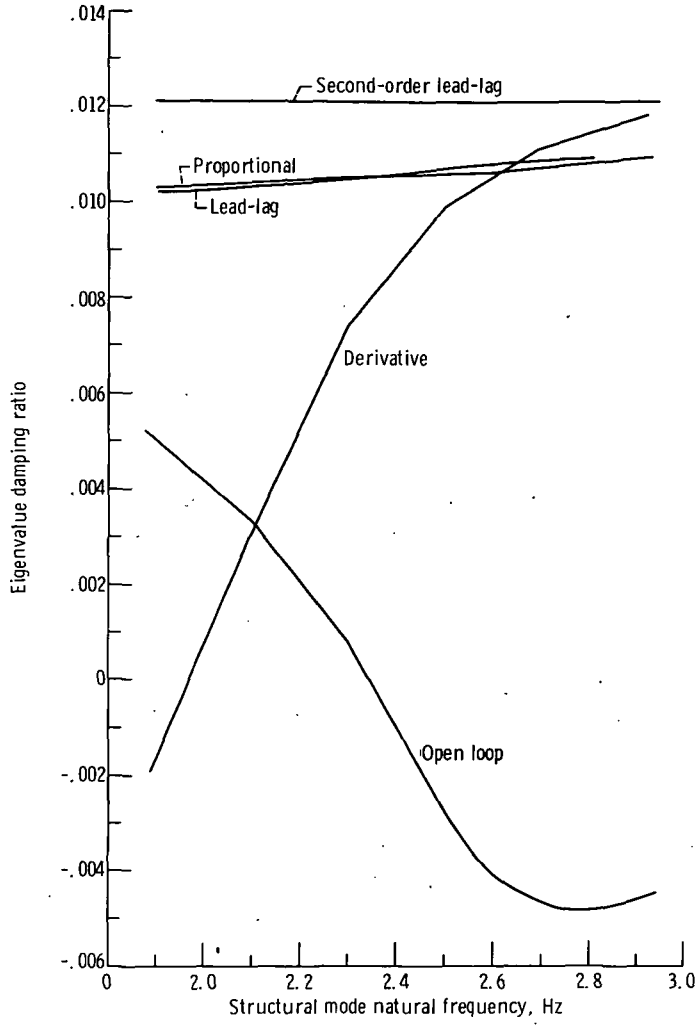

Figure 12. - Sensitivity of eigenvalue damping to variation in 2.3-hertz structural mode frequency for 90 percent of unity normalized control level controllers.

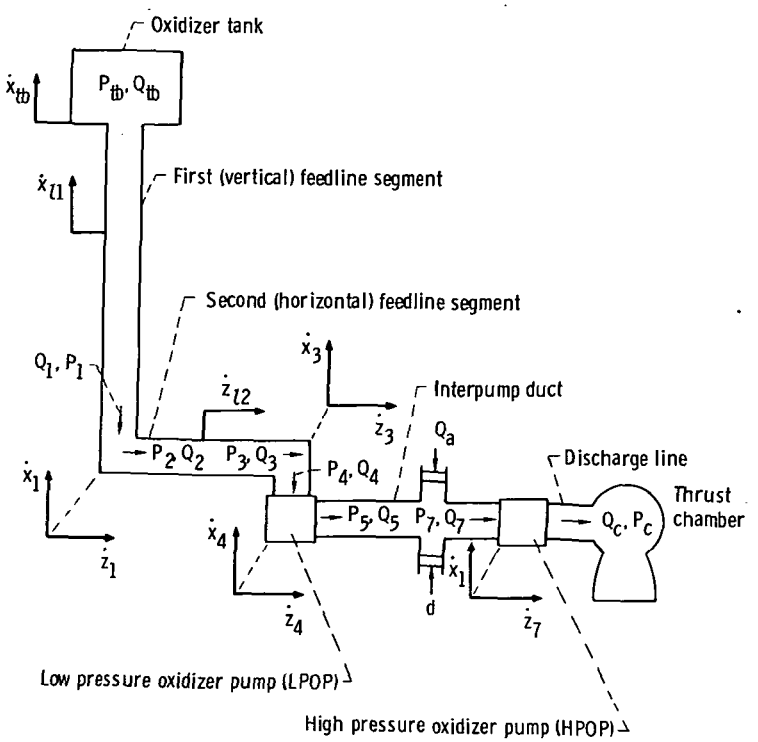

Figure 13. - Schematic of liquid oxygen system model.

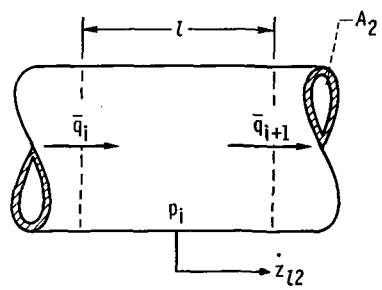

Figure 14. - Feedline control volume. (Lump length, l; pressure in i^{th} lump (second feedline), p_i; flow entering i^{th} lump (second feedline), $\bar{q}_i$; horizontal feedline velocity, $\dot{z}_{l2}$; cross sectional area (second feedline), A_2.)

NATIONAL AERONAUTICS AND SPACE ADMINISTRATION
WASHINGTON, D.C. 20546

OFFICIAL BUSINESS
PENALTY FOR PRIVATE USE $300

SPECIAL FOURTH-CLASS RATE BOOK

POSTAGE AND FEES PAID
NATIONAL AERONAUTICS AND SPACE ADMINISTRATION
451

U.S.MAIL

POSTMASTER: If Undeliverable (Section 158 Postal Manual) Do Not Return

"The aeronautical and space activities of the United States shall be conducted so as to contribute . . . to the expansion of human knowledge of phenomena in the atmosphere and space. The Administration shall provide for the widest practicable and appropriate dissemination of information concerning its activities and the results thereof."

—NATIONAL AERONAUTICS AND SPACE ACT OF 1958

NASA SCIENTIFIC AND TECHNICAL PUBLICATIONS

TECHNICAL REPORTS: Scientific and technical information considered important, complete, and a lasting contribution to existing knowledge.

TECHNICAL NOTES: Information less broad in scope but nevertheless of importance as a contribution to existing knowledge.

TECHNICAL MEMORANDUMS: Information receiving limited distribution because of preliminary data, security classification, or other reasons. Also includes conference proceedings with either limited or unlimited distribution.

CONTRACTOR REPORTS: Scientific and technical information generated under a NASA contract or grant and considered an important contribution to existing knowledge.

TECHNICAL TRANSLATIONS: Information published in a foreign language considered to merit NASA distribution in English.

SPECIAL PUBLICATIONS: Information derived from or of value to NASA activities. Publications include final reports of major projects, monographs, data compilations, handbooks, sourcebooks, and special bibliographies.

TECHNOLOGY UTILIZATION PUBLICATIONS: Information on technology used by NASA that may be of particular interest in commercial and other non-aerospace applications. Publications include Tech Briefs, Technology Utilization Reports and Technology Surveys.

Details on the availability of these publications may be obtained from:

SCIENTIFIC AND TECHNICAL INFORMATION OFFICE

NATIONAL AERONAUTICS AND SPACE ADMINISTRATION

Washington, D.C. 20546